**ORIGINAL RESEARCH**

# Model-based adaptive control of modular DAB converter for EV chargers

**Stefania Cuoghi** | **Lohith Kumar Pittala** | **Riccardo Mandrioli** | **Vincenzo Cirimele** | **Mattia Ricco** | **Gabriele Grandi**

Department of Electrical, Electronic, and Information Engineering, University of Bologna, Bologna, Italy

**Correspondence**
Riccardo Mandrioli, Department of Electrical, Electronic, and Information Engineering, University of Bologna, Viale del Risorgimento 2, 40136 Bologna, Italy.
Email: r.mandrioli@unibo.it

## Abstract

This paper presents the discrete-time modelling and control of modular input-parallel–output-parallel (IPOP) dual-active-bridge (DAB) converters for electric vehicle (EV) charging. The proposed adaptive control system ensures adequate current-sharing among parallel modules while minimizing DAB current stress by adopting dual phase-shift modulation. Driven by the growing need for fast EV charging options, the paper highlights the importance of achieving top-notch control performance, especially with varying load conditions. Specifically, it introduces a discrete-time model for adjusting controller parameters adaptively, which simplifies the typically cumbersome manual tuning process associated with these systems. The proposed PI formulae are derived to satisfy specifications on the frequency domain as phase margin and the gain crossover frequency of the open loop gain transfer function, ensuring stability and robustness in operation. Moreover, the implementation of these formulae in discrete microcontrollers facilitates seamless PI autotuning for precise current, voltage, or power control. Notably, the proposed control strategy effectively mitigates current overshot issues commonly encountered during module engagement and shedding operations in modular EV chargers. To validate its efficacy, the proposed controller is evaluated through extensive testing and comparisons within the PLECS environment, particularly focusing on a two-module IPOP-DAB converter scenario, and including comparisons with classical offline model-based pole placement methodology. Furthermore, real-time hardware-in-the-loop experiments are conducted to confirm the feasibility and performance of the proposed controller under realistic EV charging profiles.

## 1 | INTRODUCTION

Growing concerns regarding increasing air pollution and climate change due to the usage of internal combustion engine vehicles have ignited a revolution in transportation electrification [1]. This shift necessitates the development of suitable EV charging infrastructure tailored to the diverse voltage and power requirements of different EV manufacturers. Furthermore, to enable rapid charging capabilities, long-range EVs necessitate extreme fast charging (XFC) stations. This topic has been recognized as a significant research goal in recent literature [2]. Therefore, it is crucial to increase charger power ratings and develop control strategies that can adapt to any load conditions. Among the different DC/DC topologies, the DAB converter is widely adopted

for the advantages of simple structure, high power density, and the possibility to achieve soft-switching with a consequent expected high efficiency [3]. Furthermore, its symmetrical structure opens to bidirectional power flow management and the galvanic isolation guarantees a high level of protection against faults for people and devices as well as compliance with EV charging international standards (e.g. IEC 61851-23) [4].

The possibility of combining more DAB converters into modular structures (modular DAB) has been attracting a lot of attention to easily scale up or down the system based on the desired power flow. In particular, the architecture referred to as input-parallel–output-parallel (IPOP) offers the possibility of managing high-input and -output current, i.e. high-power flows [5]. Modularity is a common approach in EV charging

applications in virtue of the easier maintenance, converter reconfigurability, lower marginal cost, and improved reliability [4, 6]. Additionally, modularity allows for the usage of the highly rewarding phase-shedding (module-shedding) technique to ensure overall high-efficiency operations throughout the whole charging process [7]. In fact, the power is shared flexibly among a dynamic number of modules according to EV models and state-of-charge (SOC). However, parallel converter connection introduces significant issues. One of these is the design of the current sharing control for compensating module non-idealities mainly due to differences in the transformer parameters. These differences can lead to high levels of stress in some of the modules composing the whole architecture with a consequent increase in losses and accelerated aging [8].

Several control strategies aimed at mitigating these problems can be found in the literature. Among these, it is possible to mention the widely known average current method [9], the master-slave control, [10] and the droop control [11]. Each control strategy must be adapted to the chosen DAB modulation technique. In this regard, an overview and comparative analysis of the most popular single-phase-shift (SPS) modulation, dual-phase-shift (DPS) modulation, extended-phase-shift (EPS) modulation, and triple-phase-shift (TPS) modulation, can be found in [12]. SPS modulation is the most common control method mainly because of its simplicity. However, this technique allows for a limited range of soft-switching with a deriving back-flow power (also known as circulating power) that leads to an increase in the current stresses for switches and magnetic components with a consequent increase in losses [13]. On the other hand, the remaining phase-shift modulation techniques can offer a wider power transmission range achieving a higher level of transferred power with the same current stress than the SPS modulation [14]. Nevertheless, the required modelling and procedure for the controller design under DPS, EPS, and TPS modulations are more complex, since they require managing multiple control variables [15]. In industrial settings, the implementation of controllers in conjunction with such modulation techniques remains a relevant challenge [16]. Among the various modelling techniques available for setting controller parameters, the classical state-space averaging (SSA) technique is suitable when dealing with converters like a buck, boost, and buck-boost, where small ripples affect state variables [17]. On the other hand, for DAB converters, the generalized average modelling technique (GAM) and its improved versions are commonly employed. These methods rely on Fourier series representation to model converter waveforms, applicable across different modulation types [18]. However, the omission of higher-order frequency components in the GAM model can impact accuracy, especially in the low-frequency range [19]. This effect can be mitigated by including the third harmonic in the state variables of an improved version of the GAM model, though at the expense of increased model complexity. Meanwhile, the average value modelling (AVM) technique offers a reduced-order model for the DAB converter. Here, semiconductor switches are represented by dependent current sources, derived by averaging inductor currents over half-cycles. Overall, AVM demonstrates good accuracy in large-signal and steady-state scenarios. Nonetheless, it tends to exhibit lower accuracy in small-signal analysis at higher frequencies, increasing the control complexity, particularly with advanced modulation techniques [20]. In addition to the challenges related to the modelling of the modular converter, conventional trial and error or model-based fixed PI tuning methods often struggle to maintain satisfactory system performance beyond small deviations from the selected tuning point of the DAB converter. Uncertainties and variations in system dynamics can cause instability and poor performance of the controller [21]. This limitation is due to the nonlinearity of the converter that cannot be extracted by its linearized model [22]. Since the battery load has a large variation during the entire charging process, a smaller control gain is suitable at a low state of battery charge, while a larger control gain is suitable at fully charged conditions [21]. It follows that PI controllers based on fixed parameters cannot achieve optimal control over the entire battery charging process [21]. The model predictive control (MPC) could be a good alternative for its ability to deal with multi-objectives in a unified framework and its competitive performance over offline techniques. However, this control requires a high computational effort and high algorithmic complexity, especially in modular configurations [23]. Moreover, significant static errors may arise in output-controlled signals and power distribution when there is a substantial mismatch between the model and circuit parameters [24]. Notably, the primary factor influencing the control of modular DAB converters is the mismatch in inductance parameters. Addressing these errors typically involves either the addition of a PI regulator, despite its tendency to degrade dynamic performance, as discussed in [25], or the implementation of parameter identification algorithms aimed at accurately identifying inductance in real-time, as explored in [24]. Additionally, the control under the two constant current (CC) and constant voltage (CV) charging phases requires referring to two transfer functions and consequently, two distinct PI controllers have to be designed. Finally, the management of transient phenomena that can occur at the change between the CC and CV controllers is still an open research issue [26]. This study has several objectives. Firstly, it aims to introduce a control scheme for the inner and outer phase shift ratio control of IPOP DAB converter under DPS modulation. This scheme is designed to meet the requirements of current sharing among the modules, reduce current stress, and provide modularity towards the number of DAB modules. Secondly, the study aims to propose an adaptive model-based strategy for tuning parallel PI controllers, with each controller assigned to a module. This strategy aims to address issues encountered with conventional trial-and-error and fixed-tuning procedures. Thirdly, the study aims to develop a control strategy for seamless switching among CC, CV, and power battery charging modes, without experiencing current or voltage undershoot/overshoot. Lastly, the study aims to present a digital control mechanism for soft module engagement, disengagement, and complete module shedding throughout the battery charging process. This control mechanism is designed to improve converter efficiency by preventing output current oscillation or overshoot.

The strategy was introduced for the first time for SPS modulation of a single DAB converter under CV control in [27]. In this work, its application is extended to parallel DAB under DPS modulation owing to the ability to switch among CC, CV, and power mode control. In particular, parallel controllers, one for each module, are real-time tuned to meet the desired total output current and share it equally among the modules. To address the underperformance of fixed PI parameters previously described, real-time adjustments to the proportional–integral (PI) parameters of the controller are made based on measurements of the load droop coefficient. This dynamic tuning approach ensures the control algorithm remains effective even under large load variations during the charging process. By avoiding saturation or unstable behaviour that may result from fixed PI parameters used in manual procedures, this method enhances overall system stability and performance. The PI controller outputs are used to calculate the PWM signals under DPS modulation of each DAB converter with the help of nonlinear equations derived by Lagrange's multiplier method [16] to minimize the DAB current stress [14]. The selected form of the discrete-time controller is the PI regulator, which is widely utilized in power converter control for its robust performance, its functional simplicity, and its capability to automatically guarantee zero steady-state error on DC step response. The proposed simple discrete formulae for autotuning PI parameters exactly meet design specifications on phase margin and the corresponding crossover frequency using the so-called inversion formulae design method [28]. These formulae can be easily implemented in a control algorithm and library block and used for different types of batteries. The crossover frequency can be set based on the charging process phases to avoid current overshoot and slow step response in large and small step variations.

There are several advantages of the proposed simple discrete formulae for adaptive tuning over manual procedures. Mainly, the proposed control strategy reduces the time and effort to find a satisfactory system behaviour, since the closed-loop solution can be obtained by mathematical equations. Moreover, the proposed control allows for stability and performance analysis since it is a model-based strategy, which is not possible with manual procedures. In comparison with fixed PI parameters obtained by model-based procedures as the pole place method, the proposed adaptive control avoids unstable behaviour under different load conditions and leads to a faster step response under battery current step variation. According to load conditions, the proposed self-adaptation load change control strategy automatically selects the suitable control mode among CC, CV, and power control, while manual procedures lead to an off-line control mode. By utilizing the flexibility and ease of implementation of discrete microcontrollers, the proposed discrete algorithm implements both voltage and power controls in the form of current control where the desired battery current is derived by Kirchhoff's laws considering the voltage and power reference values. One of the major advantages of this approach is that it allows for the use of the same PI controller and tuning parameter formulae for CC, CV, and power control. Moreover, a first-order discrete filter has been used in the microcontroller to implement a new discrete soft engagement and module shedding, aimed at mitigating the current overshoots. In particular, this filter adjusts the slope of a reference signal during these operations, thereby preventing immediate engagement or shedding of the converter in response to reference current step variations.

The paper is organized as follows. The working waveforms of the process operating modes and the nonlinear small-signal model of IPOP modular DAB converters with DPS control are analysed in Section 2. Section 3 presents the proposed discrete-time model, the current sharing control strategy with reduced current stress, and autotuning PI algorithm. Test results in the PLECS simulation environment in CC, CV, and power modes under parameter variations, the comparison with other methods, and frequency analysis on Bode diagrams are discussed in Section 4. Verification through hardware-in-the-loop (HIL) results are shown in Section 5. In the last section, the conclusions derived from this work are drawn.

## 2 | BACKGROUND ON IPOP DAB UNDER DPS CONTROL

The considered IPOP DAB topology is shown in Figure 1. The structure consists of $N$ parallel modules having the same electrical parameters. This modular structure can be used explicitly in the XFC stations to reach a certain power level with lower component ratings. Input and output sides of IPOP DAB converter are characterized by the DC-bus voltage $V_{dc}$ and the EV battery voltage $V_{bat}$, respectively. The global input and output currents $i_1$ and $i_2$ are the corresponding sums of the $i$th input and output currents $i_{1i}$ and $i_{2i}$ of each module. The output capacitor $C$ is characterized by the voltage $V_c$, the current $i_c$, and the equivalent series resistance $R_c$, while the battery current is denoted as $i_{bat}$. Each DAB module is characterized by two H-bridge interconnected through a high-frequency transformer with primary and secondary voltages $v_p$ and $v_s$, and turn ratio $n$. The power transfer is given by the current $i_L$ flowing in the leakage inductor $L$. The voltage global conversion ratio is defined as $K = V_{dc}/(nV_{bat})$.

Gate signals under the considered DPS modulation are characterized by constant switching frequency $f_{sw}$ (switching period is indicated as $T_s$) and 50% duty cycle. The converter power flow in each DAB module is regulated through the inner phase shift $0 < D_1 < 1$ between H-bridge legs and the outer phase shift $0 < D_2 < 1$ between the primary and secondary H-bridge [29]. In the mind to preserve the full controllability of both phase shifts, the so-called independent surface is avoided by setting $D_1 + D_2 < 1$ [30, 31]. Therefore, the two admissible switching modes are:

- **mode 1**: $0 \leq D_1 \leq D_2 \leq 1$;
- **mode 2**: $0 \leq D_2 \leq D_1 \leq 1$.

The working waveforms under both operating modes are shown in Figure 2, while Table 1 reports $i_L$ at each switching event considering $G_1 = nV_{bat}/(4f_{sw}L)$; considering the
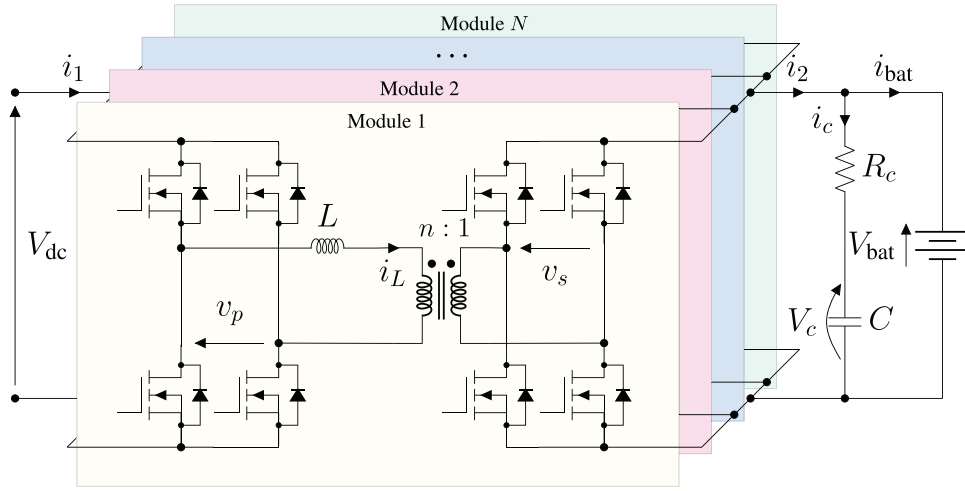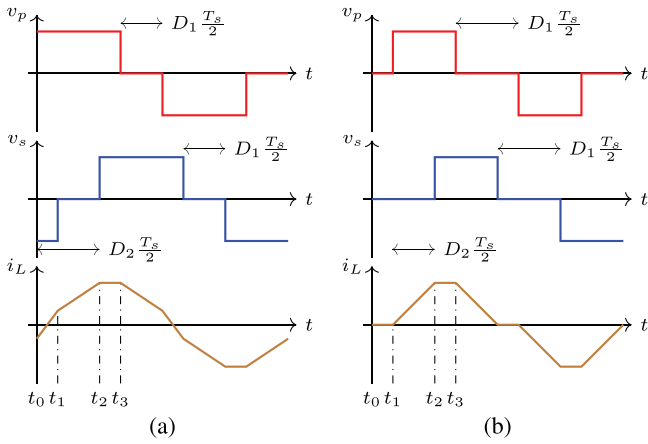
**FIGURE 1** IPOP dual active bridge converter scheme.



**FIGURE 2** DAB waveforms ($K = 1$). (a) **mode 1**; (b) **mode 2**.

**TABLE 1** Current $i_L$ at the switching instants in **mode 1** and **mode 2**.

| Time | Mode 1 | Mode 2 |
|---|---|---|
| $t_0$ | $G_1 \left[ (D_1 - 1)(K - 1) + 2(D_1 - D_2) \right]$ | $G_1 (D_1 - 1)(K - 1)$ |
| $t_1$ | $G_1 \left[ (D_1 - 1)(K - 1) - 2K(D_1 - D_2) \right]$ | $G_1 (D_1 - 1)(K - 1)$ |
| $t_2$ | $G_1 \left[ (D_1 - 1)(K - 1) + 2KD_2 \right]$ | $G_1 \left[ (D_1 - 1)(K - 1) + 2KD_2 \right]$ |
| $t_3$ | $G_1 \left[ (1 - D_1)(K - 1) + 2D_2 \right]$ | $G_1 \left[ (1 - D_1)(K - 1) + 2D_2 \right]$ |

half-wave symmetry the remaining values can be easily deduced [14]. The maximum value of $i_L$ in both modes is given by:

$$i_{\max} = \begin{cases} i_L(t_3) = G_1 \left[ (1 - D_1)(K - 1) + 2D_2 \right] & K \geq 1 \\ i_L(t_2) = G_1 \left[ (D_1 - 1)(K - 1) + 2KD_2 \right] & K \leq 1 \end{cases}. \tag{1}$$

If $K = 1$, values $i_L(t_2)$ and $i_L(t_3)$ coincide as displayed in Figure 2.

## 2.1 | The small-signal model

The nonlinear model of the converter can be derived from DAB power:

$$P = V_{\mathrm{dc}} \bar{i}_1 = V_{\mathrm{bat}} \bar{i}_2$$

$$= \frac{n V_{\mathrm{dc}} V_{\mathrm{bat}}}{4 L f_{\mathrm{sw}}} \sum_{i=1}^{N} \begin{cases} 2 D_{2i}(1 - D_{2i}) - D_{1i}^2 & \textbf{mode1} \\ D_{2i}(2 - 2 D_{1i} - D_{2i}) & \textbf{mode2} \end{cases} \tag{2}$$

where the barred variables represent the average values over a switching period of the correspondent currents [32].

From Equation (2) the converter input and output currents can be expressed as nonlinear functions of the $2N$ control variables $D_{1i}$ and $D_{2i}$ as:

$$\bar{i}_1 = \sum_{i=1}^{N} i_{1i} = \begin{cases} G_1 \sum_{i=1}^{N} \left[ 2 D_{2i}(1 - D_{2i}) - D_{1i}^2 \right] & \textbf{mode1} \\ G_1 \sum_{i=1}^{N} D_{2i}(2 - 2 D_{1i} - D_{2i}) & \textbf{mode2} \end{cases}$$
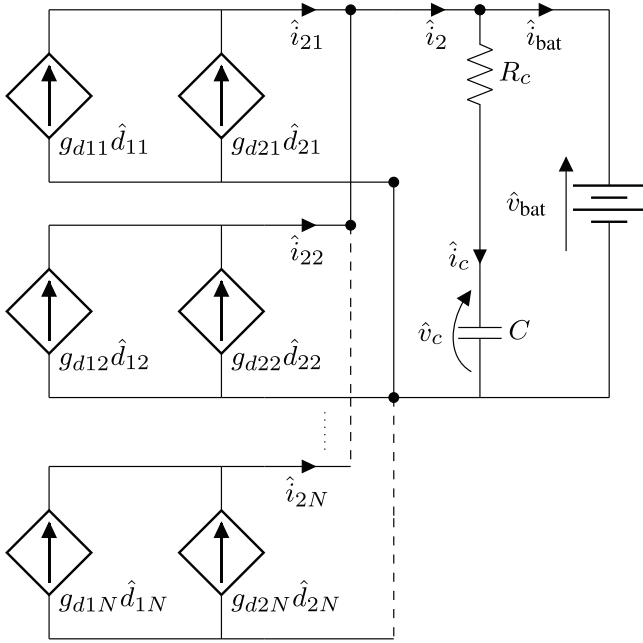
$$\bar{i}_2 = \sum_{i=1}^{N} i_{2i} = \begin{cases} G_2 \sum_{i=1}^{N} \left[ 2 D_{2i}(1 - D_{2i}) - D_{1i}^2 \right] & \textbf{mode1} \\ G_2 \sum_{i=1}^{N} D_{2i}(2 - 2 D_{1i} - D_{2i}) & \textbf{mode2} \end{cases} \tag{3}$$

$$G_1 = \frac{n V_{\mathrm{bat}}}{4 f_{sw} L}, \qquad G_2 = \frac{n V_{\mathrm{dc}}}{4 f_{sw} L}.$$

When $D_{1i} = 0$ and $D_{2i} = 0.5$ output current $\bar{i}_2$ reaches its maximum value $N G_2 / 2$; this coincides with SPS operations.

Assuming that input and output voltage perturbations are negligible, the small-signal output current can be written as:

$$\hat{i}_2(t) = \sum_{i=1}^{N} \left( g_{d1i} \hat{d}_{1i} + g_{d2i} \hat{d}_{2i} \right) \tag{4}$$

**FIGURE 3** Small-signal model of the battery section of the IPOP DPS-DAB converter system.

having:

$$g_{d1i} = \left.\frac{\hat{i}_{2i}}{\hat{d}_{1i}}\right|_{\hat{d}_{2i}=0} = \begin{cases} -2G_2D_{1i} & \textbf{mode1} \\ -2G_2D_{2i} & \textbf{mode2} \end{cases} \quad (5)$$

$$g_{d2i} = \left.\frac{\hat{i}_{2i}}{\hat{d}_{2i}}\right|_{\hat{d}_1=0} = \begin{cases} 2G_2(1-2D_{2i}) & \textbf{mode1} \\ 2G_2(1-D_{1i}-D_{2i}) & \textbf{mode2} \end{cases} \quad (6)$$

where $\hat{d}_{1i}$ and $\hat{d}_{2i}$ are the small-signal inner and outer phase shift of the $i$th DAB module. A visual representation of the small-signal model is available in Figure 3.

# 3 | PROPOSED CONTROL MODEL AND STRATEGY

The main idea of the proposed control procedure is to consider the desired values of output currents $\bar{i}_{2i}^*$ of each DAB converter as the discrete control output variables rather than the PWM phase shift ratio $D_{1i}$ and $D_{2i}$. Considering the Thévenin model of the battery shown in Figure 4, where $V_{oc}$ denotes the battery open circuit voltage while $R$ is the droop coefficient, the discrete-time system to be controlled has the following linear transfer function:
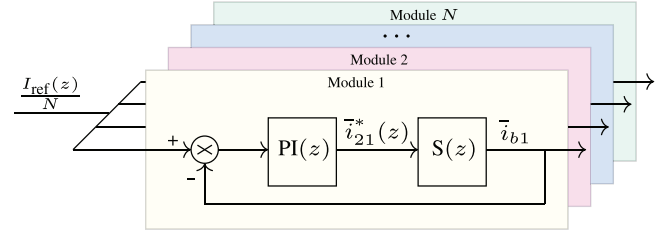
$$S(z) = \frac{\bar{i}_{bat}(z)}{\bar{i}_2(z)} = \frac{R_c}{R+R_c}\frac{z-\beta}{z-\alpha}, \quad (7)$$

having:

$$\alpha = e^{-\frac{T_s}{C(R+R_c)}}; \quad \beta = \frac{(R+R_C)\alpha-R}{R_C}. \quad (8)$$
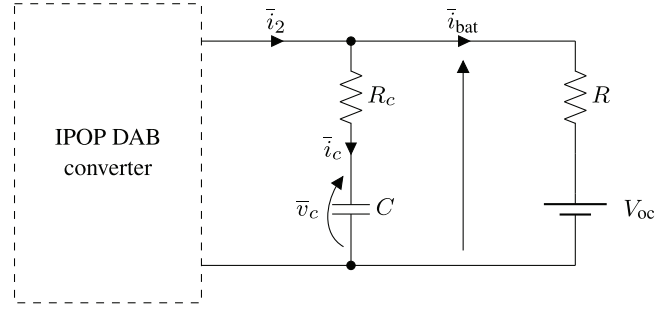


**FIGURE 4** Output circuit with the Thévenin model of the battery.



**FIGURE 5** The proposed control structure with current sharing strategy for PI design.

Equation (7) has been originated by the Z-transform of a zero-order hold:

$$H(s) = \frac{1-e^{-T_s s}}{s}, \quad (9)$$

with sampling time $T_s$ and the continuous-time model:

$$S(s) = \frac{\bar{i}_{bat}(s)}{\bar{i}_2(s)} = \frac{R_c}{R+R_c}\frac{s+b}{s+a}, \quad (10)$$

having:

$$a = \frac{1}{C(R+R_c)}, \quad b = \frac{1}{CR_C}, \quad (11)$$

which has been derived by the circuit Kirchhoff's laws of the output circuit shown in Figure 4, similarly to what is shown in [27].

The proposed control scheme ensures that each IPOP DAB module achieves equal current sharing by implementing parallel controllers, with one controller assigned to each module as depicted in Figure 5. The control signals for each converter are adjusted differently, such that the share of battery current $\bar{i}_{bi}$ provided by each module tracks $I_{ref}/N$. The following equation:

$$\bar{i}_{bi} = \bar{i}_{bat}\frac{\bar{i}_{2i}}{\bar{i}_2}, \quad (12)$$

establishes the relationship between the module currents $\bar{i}_{2i}$ and the corresponding fraction of battery current $\bar{i}_{bi}$, which can be expressed as $\bar{i}_{bi} = S(z)\bar{i}_{2i}$, following the superposition principle mentioned in [33]. A good current sharing is achieved when all the currents $\bar{i}_{bi}$ are equal to $I_{ref}/N$.

In the case of CC charging mode, $I_{ref}$ directly represents the desired charging current. On the other hand, CV operations or yield power control are achieved by setting:

$$I_{ref} = \frac{V_{ref} - V_{oc}}{R}, \tag{13}$$

$$I_{ref} = \frac{\sqrt{V_{oc}^2 + 4RP_{ref}} - V_{oc}}{2R}, \tag{14}$$

having $V_{ref}$ and $P_{ref}$ as the intended charging voltage and power respectively, while the droop coefficient $R$ is estimated as:

$$R = \frac{V_{bat} - V_{oc}}{I_{bat}}. \tag{15}$$

The selected discrete-time PI controller presents the form:

$$PI(z) = K_P + K_I \frac{z + 1}{z - 1}. \tag{16}$$

The corresponding frequency response can be written in polar and Cartesian forms as follows:

$$PI(\omega, T_s) = M(\omega, T_s)e^{j\varphi(\omega, T_s)} = K_P - j\left[\frac{K_I}{\tan\left(\frac{\omega T_s}{2}\right)}\right], \tag{17}$$

where $M(\omega, T_s)$ and $\varphi(\omega, T_s)$ are the magnitude and the phase of $PI(\omega, T_s)$. Since the model (7) is a type zero system, the steady-state requirement is satisfied by the pole at $-1$ of the controller. The two PI parameters can be used to meet specifications on the phase margin $\phi_m$ and the gain crossover frequency $\omega_g$ using the Inversion Formulae method discussed in [34]. This means that the magnitude and the phase of the loop gain frequency response $L(\omega, T_s) = PI(\omega, T_s) S(\omega, T_s)$ have to be equal to 1 and $\pi + \phi_m$ at frequency $\omega_g$:

$$\begin{aligned} \left|L(\omega_g, T_s)\right| &= 1 \\ \angle L(\omega_g, T_s) &= \pi + \phi_m \end{aligned}. \tag{18}$$

The frequency response of Equation (7) can be written in the Cartesian form:

$$\begin{aligned} S(\omega, T_s) &= \frac{R_c}{R + R_c} \frac{e^{j\omega T_s} - \beta}{e^{j\omega T_s} - \alpha} = \\ &= \frac{R_c}{R + R_c} \frac{\cos(\omega T_s) - \beta + j\sin(\omega T_s)}{\cos(\omega T_s) - \alpha + j\sin(\omega T_s)} = \\ &= R_c \frac{1 + \alpha\beta - (\alpha + \beta)\cos(\omega T_s) + j(\beta - \alpha)\sin(\omega T_s)}{(R + R_c)(1 + \alpha^2 - 2\alpha\cos(\omega T_s))}. \end{aligned} \tag{19}$$

It follows that:

$$\left|S(\omega, T_s)\right| = \frac{R_c}{R + R_c}\sqrt{\frac{1 + \beta^2 - 2\beta\cos(\omega T_s)}{1 + \alpha^2 - 2\alpha\cos(\omega T_s)}}.$$

$$\angle S(\omega, T_s) = \tan^{-1}\left[\frac{(\beta - \alpha)\sin(\omega T_s)}{1 + \alpha\beta - (\alpha + \beta)\cos(\omega T_s)}\right] \tag{20}$$

From Equation (18) the PI controller has to be designed in such a way that its magnitude and phase at frequency $\omega_g$ are equal to

$$M_g = \frac{1}{\left|S(\omega_g, T_s)\right|}, \tag{21}$$

$$\varphi_g = \phi_m - \pi - \angle S(\omega, T_s)$$

meaning that:

$$PI(\omega_g, T_s) = M_g(\omega_g, T_s)e^{j\varphi_g(\omega_g, T_s)} \tag{22}$$

holds. By equating the real and imaginary parts of both sides of Equations (17) and (22), the following equations are obtained:

$$M_g \cos\varphi_g = K_P \tag{23}$$

$$M_g \sin\varphi_g = -\frac{K_I}{\tan\left(\frac{\omega_g T_s}{2}\right)}. \tag{24}$$

Solving Equations (23) and (24) with respect to the PI parameters, the following relations can be derived:

$$\begin{aligned} K_P &= \frac{R + R_C}{R_C}\sqrt{\frac{1 + \alpha^2 - 2\alpha\cos(\omega_g T_s)}{1 + \beta^2 - 2\beta\cos(\omega_g T_s)}}\cos\varphi_g \\ K_I &= -K_P \tan\frac{\omega_g T_s}{2}\tan\varphi_g \end{aligned}, \tag{25}$$

where

$$\varphi_g = \phi_m - \pi - \tan^{-1}\left[\frac{(\beta - \alpha)\sin(\omega_g T_s)}{1 + \alpha\beta - (\alpha + \beta)\cos(\omega_g T_s)}\right], \tag{26}$$

assuming that $K_P > 0$ and $K_I > 0$.

## 3.1 | Dual phase shift control with reduced current stress

The proposed control strategy for inner and outer phase shift ratio control with reduced current stress is shown in Figure 6. The PI parameters are dynamically computed in real-time by utilizing Equation (25) within the specified design constraints to determine the desired values of $\bar{i}_{2i}$. However, according to Equation (3), there are infinite combinations of $(D_1, D_2)$ in DPS control to track a required value of $\bar{i}_{2i}$. To find the unique combination of $(D_1, D_2)$ that meets the desired value of $\bar{i}_{2i}$ with minimum DAB current, the approach of Lagrange's multipliers is adopted. It follows that the inner and outer phase shifts
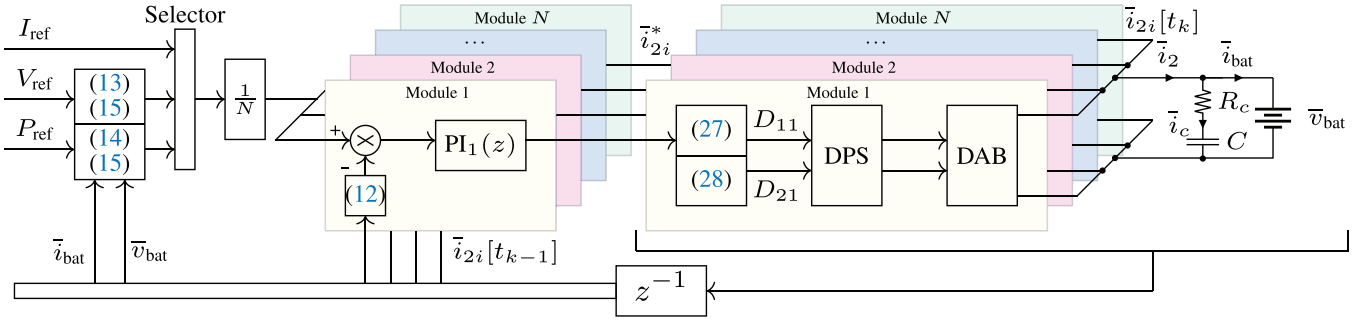
**FIGURE 6** Proposed control scheme for inner and outer phase shift ratio control with reduced current stress.

are calculated using the following nonlinear relationships as a function of $\bar{i}_{2i}$:

$$
K \geq 1 \quad
\begin{cases}
D_{1i} = \begin{cases}
1 - (K+1)\sqrt{\dfrac{\bar{i}_{2i}/G_2}{K^2 + 2K - 3}} & 0 \leq \bar{i}_{2i} < \gamma_1 \\[4mm]
(K-1)\sqrt{\dfrac{1 - 2\bar{i}_{2i}/G_2}{2K^2 - 4K + 6}} & \gamma_1 \leq \bar{i}_{2i} \leq \dfrac{G_2}{2}
\end{cases} \\[12mm]
D_{2i} = \begin{cases}
(K-1)\sqrt{\dfrac{\bar{i}_{2i}/G_2}{K^2 + 2K - 3}} & 0 \leq \bar{i}_{2i} < \gamma_1 \\[4mm]
\dfrac{1}{2} - \sqrt{\dfrac{1 - 2\bar{i}_{2i}/G_2}{2K^2 - 4K + 6}} & \gamma_1 \leq \bar{i}_{2i} \leq \dfrac{G_2}{2}
\end{cases}
\end{cases}
$$

$$
\gamma_1 = \frac{G_2(K+3)(K-1)}{4K^2}; \tag{27}
$$

$$
K \leq 1 \quad
\begin{cases}
D_{1i} = \begin{cases}
1 - (K+1)\sqrt{\dfrac{\bar{i}_{2i}/G_2}{1 - 3K^2 + 2K}} & 0 \leq \bar{i}_{2i} < \gamma_2 \\[4mm]
(1-K)\sqrt{\dfrac{1 - 2\bar{i}_{2i}/G_2}{6K^2 - 4K + 2}} & \gamma_2 \leq \bar{i}_{2i} \leq \dfrac{G_2}{2}
\end{cases} \\[12mm]
D_{2i} = \begin{cases}
(1-K)\sqrt{\dfrac{\bar{i}_{2i}/G_2}{1 - 3K^2 + 2K}} & 0 \leq \bar{i}_{2i} < \gamma_2 \\[4mm]
\dfrac{1}{2} - K\sqrt{\dfrac{1 - 2\bar{i}_{2i}/G_2}{6K^2 - 4K + 2}} & \gamma_2 \leq \bar{i}_{2i} \leq \dfrac{G_2}{2}
\end{cases}
\end{cases}
$$

$$
\gamma_2 = \frac{G_2(3K+1)(1-K)}{4}. \tag{28}
$$

In particular, Equations (27) and (28) have been derived by the solution of the system:

$$
\begin{cases}
\dfrac{\partial \mathcal{L}}{\partial \lambda} = 0 \\[3mm]
\dfrac{\partial \mathcal{L}}{\partial D_{1i}} = 0 \\[3mm]
\dfrac{\partial \mathcal{L}}{\partial D_{2i}} = 0
\end{cases} \tag{29}
$$

where $\mathcal{L}$ is the Lagrangian function (30) derived from Equations (1) and (3).

## 4 | PLECS SIMULATION RESULTS

The CC–CV charging procedure is the most widely used battery charging procedure. The battery is charged at a constant current until the voltage reaches the cut-off value. Following that, the constant voltage is maintained under the CV mode control until the battery reaches the desired SOC [35]. By considering this charging procedure, the proposed control scheme illustrated in Figure 6 has been tested in the PLECS (Plexim GmbH) simulation tool referring to a two-module IPOP DAB converter whose parameters are listed in Table 2. The discrete PI block available in the PLECS library is used by adopting the trapezoidal integration method in all the closed-loop controls. The

$$
K \geq 1 \quad \mathcal{L}(D_{1i}, D_{2i}, \lambda) = G_1[D_{1i}(1-K) + 2D_{2i} + K - 1] + \lambda
\begin{cases}
G_2[-D_{1i}^2 + 2D_{2i}(1 - D_{2i})] - \bar{i}_{2i} & \textbf{mode1} \\[2mm]
G_2 D_{2i}(2 - 2D_{1i} - D_{2i}) - \bar{i}_{2i} & \textbf{mode2}
\end{cases}
$$

$$
K \leq 1 \quad \mathcal{L}(D_{1i}, D_{2i}, \lambda) = G_1\big[(D_1 - 1)(K - 1) + 2KD_2\big] + \lambda
\begin{cases}
G_2[-D_{1i}^2 + 2D_{2i}(1 - D_{2i})] - \bar{i}_{2i} & \textbf{mode1} \\[2mm]
G_2 D_{2i}(2 - 2D_{1i} - D_{2i}) - \bar{i}_{2i} & \textbf{mode2}
\end{cases}
$$

$$
\tag{30}
$$

**TABLE 2** Parameter values of the IPOP DAB converter scheme.

| Symbol | Parameter | Value | Units |
|--------|-----------|-------|-------|
| $V_{dc}$ | DC bus voltage | 800 | V |
| $V_{bat}$ | Battery voltage | 400 | V |
| $R$ | Internal cell resistance | 2 | m$\Omega$ |
| $C$ | Filter capacitance | 50 | mF |
| $R_c$ | Series resistance | 1 | m$\Omega$ |
| $L$ | Leakage inductance | 41 | $\mu$H |
| $n$ | Transformer ratio | 2 | - |
| $f_{sw}$ | Switching frequency | 20 | kHz |
| $T_s$ | Sampling time | 50 | $\mu$s |
| $N$ | Parallel DAB number | 2 | - |

**TABLE 3** Comparison results under design specification: $\phi_m = 90°$.

| Parameters | Classical | Proposed |
|------------|-----------|----------|
| $\phi_m$ | 89° | 90° |
| $\omega_g$ | 4.12 rad/s | 2000 rad/s |
| $K_P$ | 0.67 | Adaptive |
| $K_I$ | 4 | Adaptive |
| Settling time | >1 s | 1.8 ms |

PI parameters are calculated in real-time through the function blocks that implement discrete equations (25) and (26) and are provided externally to the discrete PI block. This procedure is referred to as an auto-tuning of the PI parameters. In this calculation, a gain of $2/T_s$ is added to the integral constant ($K_I$ term) to adjust the difference between Equation (16) and the chosen PLECS controller form. To ensure robust stability, a generous phase margin of $\phi_m = 90°$ has been chosen, while the gain crossover frequency $\omega_g$ is adjusted based on the phase of the charging process. The real-time computation of the droop coefficient $R$ relies on the measured signals of output voltage and current as per Equation (15). For estimating the $V_{OC}$, a lookup table method based on the battery SOC can be employed, as detailed in [36]. The values of $D_{1i}$ and $D_{2i}$ are determined by Equations (27) and (28), with switches selecting $D_{1i}$ and $D_{2i}$ values according to the relevant permissible ranges and the output of the PI controller.

## 4.1 | CC mode control

The effectiveness of the proposed control has been firstly tested in CC mode under $I_{ref}$ step variation from 0 to 120 A and 120 to 150 A, meeting $\phi_m = 90°$, $\omega_g = 900$ rad/s, and $\omega_g = 2000$ rad/s, respectively, in the case of SOC equal to 70%. Different values of $\omega_g$ avoid current overshoot in the first large step variation and slow step response in the second small step variation.

The corresponding CC mode control results are shown from Figure 7–9. In particular, Figure 7 shows the two-step responses of battery current $i_{bat}$, roughly estimating the settling time as 4 ms, and 1.8 ms in large and small step variation, respectively. Similar considerations can be drawn from the inductor currents shown in Figure 8. Figure 9 depicts the real-time computed droop coefficient $R$ with respect to the $\omega_g$ variation, where the auto-tuning of PI parameters can be observed as per Equation (25).

To verify the main advantage of the real-time computed droop coefficient $R$ and the auto-tuning of the PI parameters to work optimally even under large parameter variations,

the proposed controller has been tested under different initial SOCs. The battery currents with SOC = 70% and SOC = 20% are shown in Figure 10. As can be seen, the same waveforms have been obtained in transient conditions showcasing the controller's adequate robustness.

To further understand the effectiveness of the proposed method, a comparison with one of the conventional controls has been investigated. In particular, a comparison with model-based fixed PI parameters obtained using the classical pole placement method [37] and the resistive battery model have been studied along with the battery parameter variations.

Since the resistance in this model varies significantly during the charging process, its value has been assumed to be equal to the battery droop under fully charged conditions, as in conventional offline tuning methods. Setting $R = V_c/I_{ref} = 3.3\Omega$, $\zeta = 1.3$, $\omega_n = 700$ rad/s, the obtained PI controller parameters $K_P = 330$, $K_I = 90000$ lead $\bar{i}_{2i}$ out of the admissible safety range, nerveless the frequency characteristics $\phi_m = 88°$, $\omega_g = 2000$ rad/s are close to the given requirements. It follows that the considered specifications have been reduced to $\omega_n = 5$ rad/s, and $\zeta = 1$ to maintain the previous phase margin ($\phi_m = 89°$, $\omega_g = 4.12$ rad/s) leading to $K_P = 0.67$, and $K_I = 4$. The corresponding settling time has been increased from roughly 1.8 ms with the proposed control to more than 1 s in the classical method as shown in Figure 11. The main comparison results under the batter current 120 to 150 A variation and $\phi_m = 90°$ are shown in Table 3.

Since an increment in the internal cell resistance $R_{in}$ refers to the battery aging, other tests have been held to verify the proposed control under $R_{in}$ variation from 2 to 20 m$\Omega$. The battery current $i_{bat}$ step variation from 120 to 150 A in the case of SOC equal to 70% with the previous PI designs are shown in Figure 12. In contrast to the fixed PI parameter method, the battery current step response has not been affected by the considered parameter variation with the proposed method. Notice that the internal cell resistance $R_{in}$ is a crucial parameter in the EV battery model, directly impacting the droop coefficient $R$. Therefore, real-time measurements of the droop coefficient $R$ are employed to detect fluctuations in $R_{in}$. These variations are then compensated by adjusting the controller parameters.

To further verify the capability of the proposed control, the same $R_{in}$ parameter depicted in Figure 12 is also considered with a two-series battery pack reaching the voltage level 800 V. In this case, as the voltage global conversion ratio is leading to $K \leq 1$, the inner and outer phase shifts are computed by Equation (28). The good results shown in Figure 13 confirm that
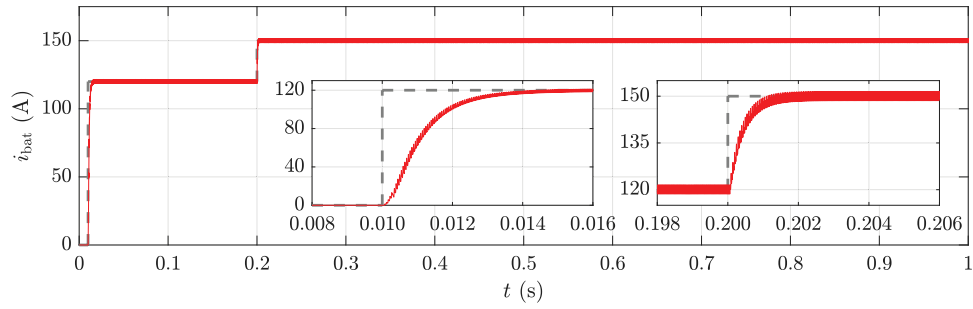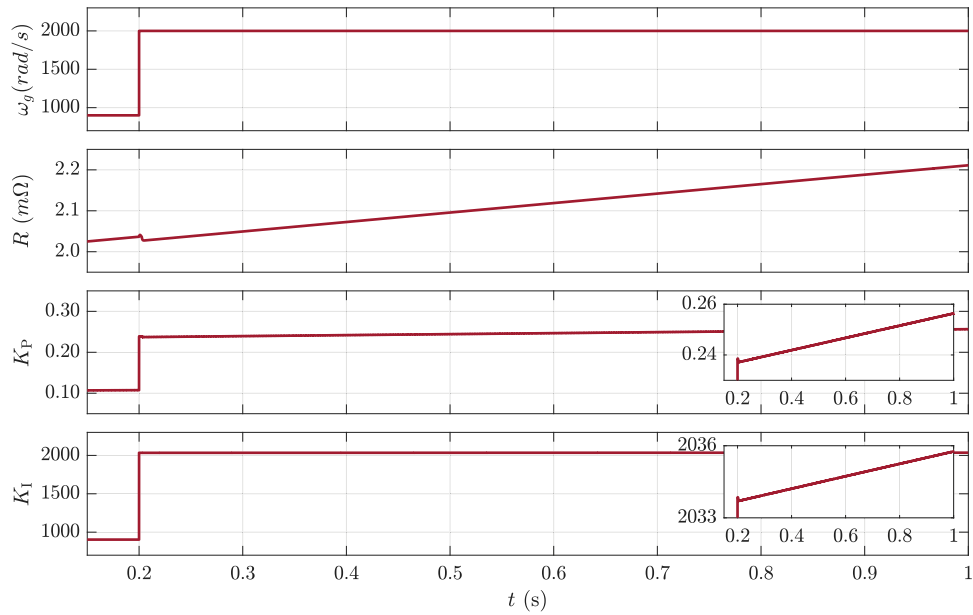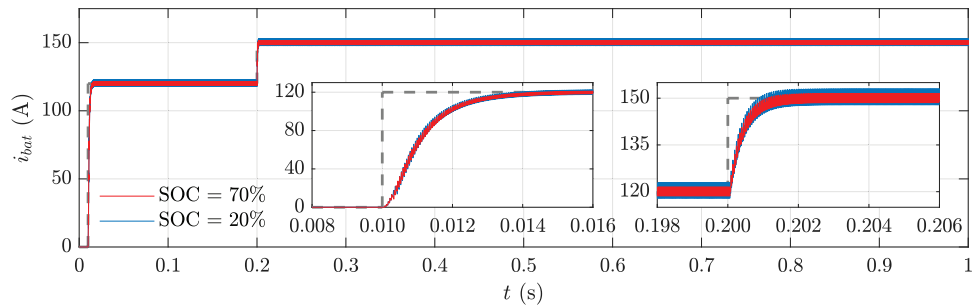
**FIGURE 7**   Battery current 0–120 A and 120–150 A step variation under $\phi_m = 90°$, $\omega_g = 900$ rad/s, and $\omega_g = 2000$ rad/s, respectively.
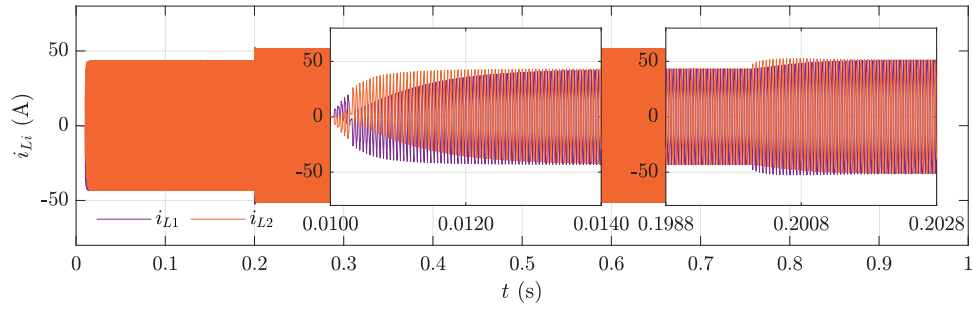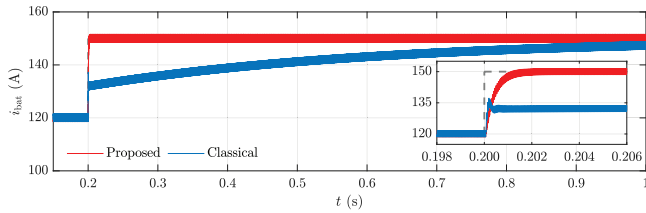


**FIGURE 8**   Inductor currents 0–120 A and 120–150 A step variation under $\phi_m = 90°$, $\omega_g = 900$ rad/s, and $\omega_g = 2000$ rad/s, respectively.
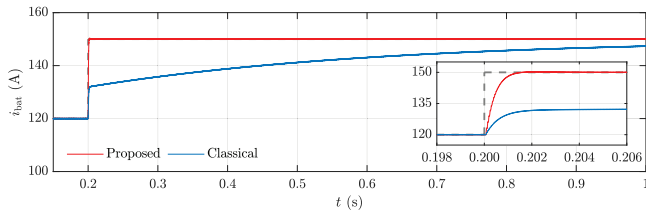


**FIGURE 9**   PI parameters auto-tuning during 120–150 A step variation.



**FIGURE 10**   Battery current with SOC = 70% and SOC = 20% during 0–120 A and 120–150 A step variation.

**FIGURE 11**   Battery current 120–150 A step variation under $\phi_\mathrm{m} = 90°$, $\omega_\mathrm{g} = 2000$ rad/s with the proposed method and $\omega_\mathrm{n} = 5$, and $\zeta = 1$ with classical method.



**FIGURE 12**   Battery current 120–150 A step variation in the case of $R_\mathrm{in} = 20$ m$\Omega$ under $\phi_\mathrm{m} = 90°$, $\omega_\mathrm{g} = 2000$ rad/s with the proposed method and $\omega_\mathrm{n} = 5$, and $\zeta = 1$ with classical method.
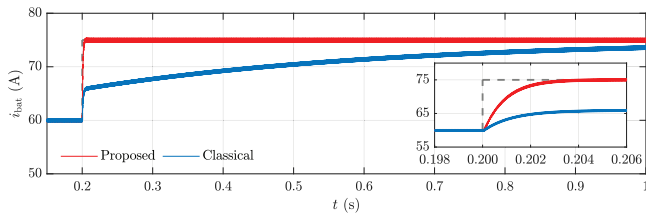


**FIGURE 13**   Battery current 120–150 A step variation in the case of two series battery pack and $R_\mathrm{in} = 20$ m$\Omega$ under $\phi_\mathrm{m} = 90°$, $\omega_\mathrm{g} = 2000$ rad/s with the proposed method and $\omega_\mathrm{n} = 5$, $\zeta = 1$ with classical method.

the proposed algorithm can be used for different EV batteries without modifications.

## 4.2 | Current sharing control verification

The proposed method has been tested under two different inductance values to verify the effectiveness of the current sharing control and compare it with the average control. This has been achieved by tuning the PI controller considering the average model of the IPOP converter. The two-module IPOP-DAB PWM modulation signals have been generated by halving PI output. In particular, the main IPOP converter waveforms with $L_1 = 41\,\mu$H and $L_2 = 45.1\,\mu$H (10% inductance mismatch) under 120 to 150 A step variation is shown in Figure 14 with and without proposed current sharing compensation. As can be seen, even though there are mismatches in the inductance values, the current sharing is well achieved in the transient and steady-state conditions with the proposed control nullifying current deviation visible in Figure 14(a).

## 4.3 | CV control mode

The battery current gradually drops from the nominal value to close to zero during CV control mode. As all converter parameters change slowly, this test segment just considers the CC–CV mode changeover. This transition is still an open control issue that necessitates a precise method to reduce the possibility of over-voltage charging [38]. The proposed control meeting $\phi_\mathrm{m} = 90°$, $\omega_\mathrm{g} = 2000$ rad/s has been tested and compared with two parallel PI controller topologies, as in [39] and [40], and using average CC-CV mode control. The current and voltage reference values are set as 120 A and 391.1 V, respectively, which is the battery voltage value at the switching instant. Figure 15 depicts that the parallel PI architecture yields an undershoot in output voltage at the switching instant due to the integral effect of the voltage PI controller since the $V_\mathrm{ref} - V_\mathrm{bat}$ error is not equal to zero before the commutation. This effect is avoided by using the same PI controllers for both modes changing the reference current value, as shown in Figure 6.

## 4.4 | Power control and soft module engagement/shedding

To better emphasize the proposed controller performance and versatility, power charge mode control has been tested using the proposed control scheme shown in Figure 6. Since in low-power conditions a single module leads to a higher efficiency than two or more modules, the proposed control has been tested to verify the possibility of soft engagement and shedding [7].

Using the parameters collected in Table 2, the maximum power that each DAB module can handle is calculated as per the power equation given in [31]. A ramp signal has been selected to match the rated power of each DAB module and is used as the reference input for the controller, enabling the output power adjustment in accordance with the system requirements. To automatize the on-off power switch of the second DAB converter, a relay has been chosen with a certain threshold value, i.e. half the rated power with $\pm2.5$ kW hysteresis band, setting the upper and lower limits for enabling and disabling the PWM signals of the second parallel DAB. A digital filter has been introduced after the relay to reduce the current overshoot in the switching transient [41]. In particular, the reference currents $I_{\mathrm{ref}1,2}$ of the two converters are computed by:

$$I_\mathrm{ref1}(z) = \frac{I_\mathrm{ref}(z)}{2}\left[1 + P(z)\frac{z+1}{z(1+a)+1-a},\right] \quad (31)$$

$$I_\mathrm{ref2}(z) = \frac{I_\mathrm{ref}(z)}{2}\left[1 - P(z)\frac{z+1}{z(1+a)+1-a},\right] \quad (32)$$

where $P(z)$ is the relay power control signal, $a = 2\tau/T_\mathrm{s}$ and $\tau$ is the filter time constant. Figures 16 and 17 show the achievement of soft engagement and shedding of the second parallel DAB converter during the simulations. As noticed, the converter output currents are not affected by the engagement and disengagement procedure, even if the step current variation
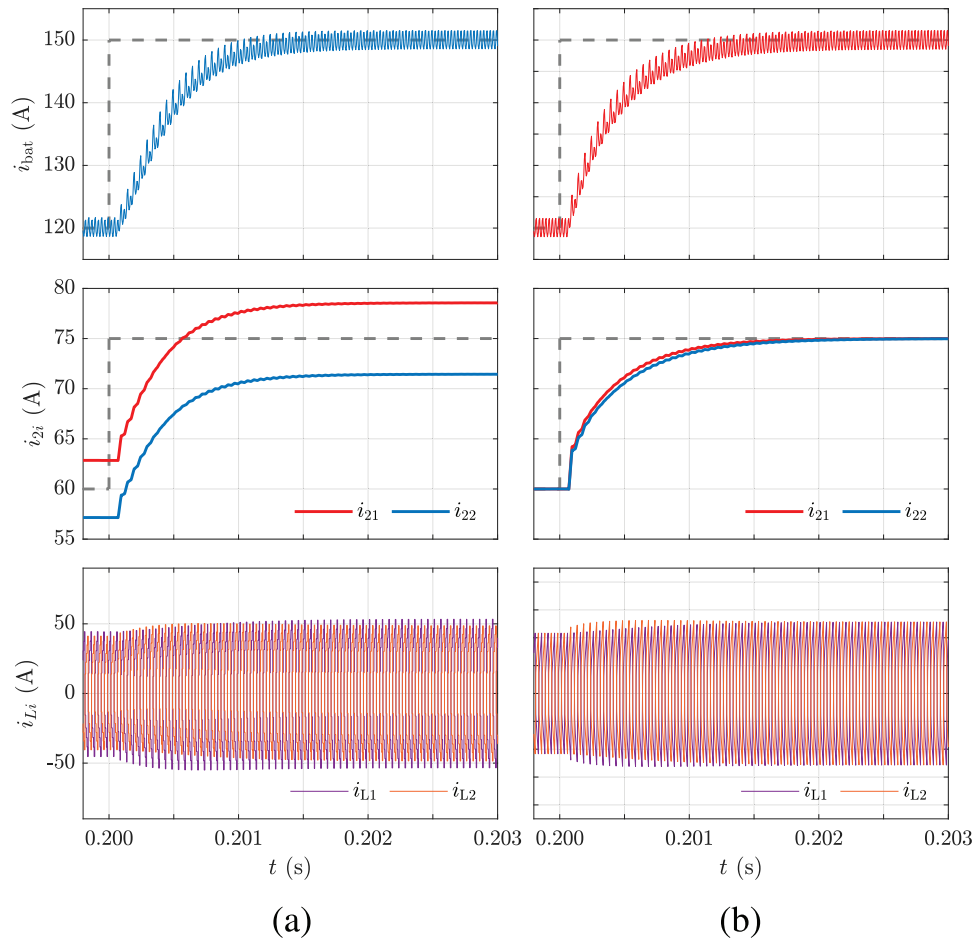
**FIGURE 14**    Two-module IPOP DAB $i_{bat}$, $i_{2i}$, and $i_{Li}$ waveforms under 120–150 A step variation with $L$ discrepancies, using average control (a) without current sharing compensation and (b) with the proposed control.
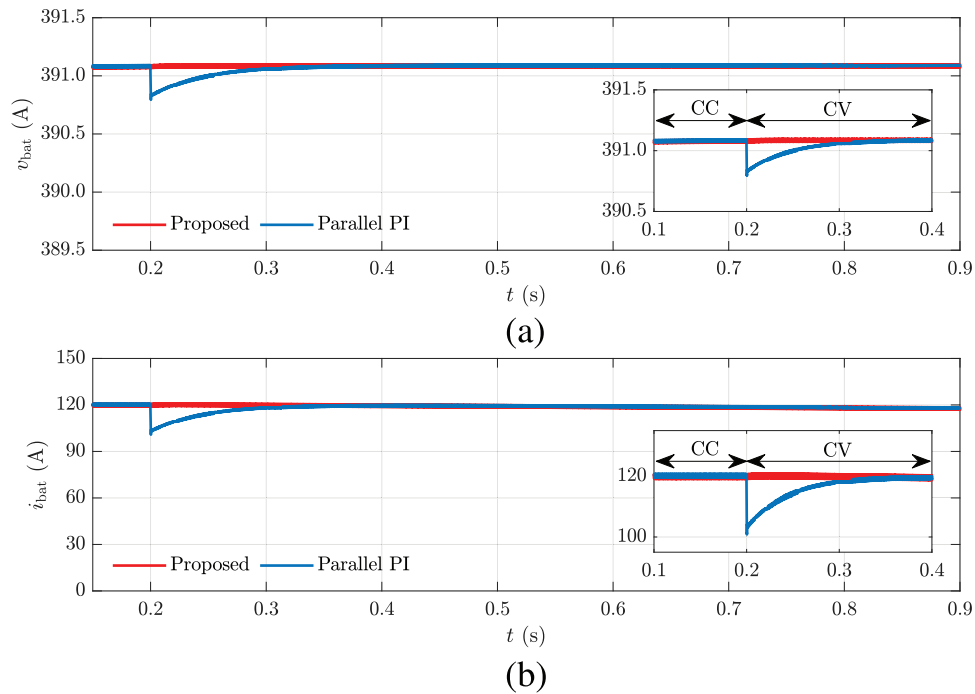


**FIGURE 15**    CC–CV mode switch: (a) battery output voltage; (b) current with the proposed method and with two parallel PI controllers.
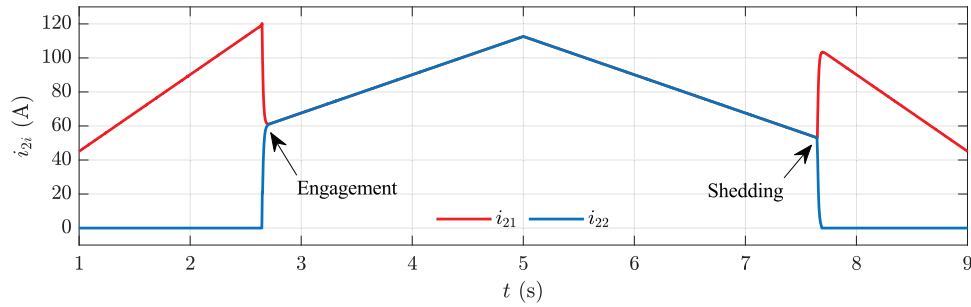
**FIGURE 16**    Soft-engagement and shedding of the second DAB parallel converter output currents with the proposed control.
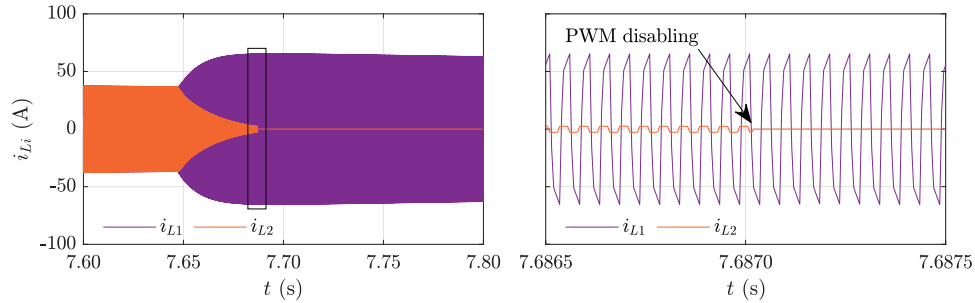


**FIGURE 17**    Inductor currents during module shedding of the second DAB.

in the first converter doubles. In Figure 17 referring to the inductor currents, the left side plot clearly depicts the module shedding process whereas the zoom on the right side shows the PWM disabling where a complete module shutdown takes place.

## 4.5 | Frequency analysis

The stability analysis of the controlled system has been carried out through the Z-domain Bode plots. The green lines in Figure 18 refer to the Bode plots of the discrete-time system:

$$S(z) = \frac{0.33z - 0.05}{z - 0.72}, \tag{33}$$

with the system parameters shown in Table 2. The PI controller expressions obtained using the proposed method and meeting zero position error, $\phi_m = 90°$, $\omega_g = 900$ rad/s, and $\omega_g = 2000$ rad/s respectively are:

$$PI_1(z) = \frac{0.128z - 0.083}{z - 1}, \tag{34}$$

$$PI_2(z) = \frac{0.285z - 0.183}{z - 1}. \tag{35}$$

The Bode plots of the loop gain frequency responses $L_{1,2}(\omega, T_s) = S(\omega, T_s)PI_{1,2}(\omega, T_s)$ for $\omega$ in $[0, \pi / T_s]$ and sampling period $T_s$ are shown in blue and dashed red lines in Figure 18. Notice that the constraints are exactly satisfied.

Table 4 summarizes the advantages and limitations of the proposed control vs classical method.

**TABLE 4**    Advantages and limitation of the proposed control vs classical method.

| Type of control | Advantages | Limitation |
|---|---|---|
| Classical | Low implementation complexity | PI saturation issues |
| | Well known technique | Slow dynamic performance |
| Proposed | Better dynamic performance | Medium implementation complexity |
| | Robustness against load variation and battery aging | Higher cost for $R$ measurement |
| | Effective current sharing compensation | |
| | Less time and effort to achieve a satisfactory system | |

## 5 | VERIFICATION THROUGH HARDWARE-IN-THE-LOOP

To assess the real-time feasibility of the CC–CV, and power charge mode control methods discussed in Section 4, hardware-in-the-loop (HIL) tests were performed. The experimental setup for real-time HIL is depicted in Figure 19. In this setup, the DAB converter is emulated using the RT-box 1 (Plexim GmbH), while the controller is emulated using the Delfino TMS320F28379D controlCARD R1.3 (Texas Instruments Incorporated) digital signal processor (DSP). The execution codes for both the RT-box 1 and DSP were developed
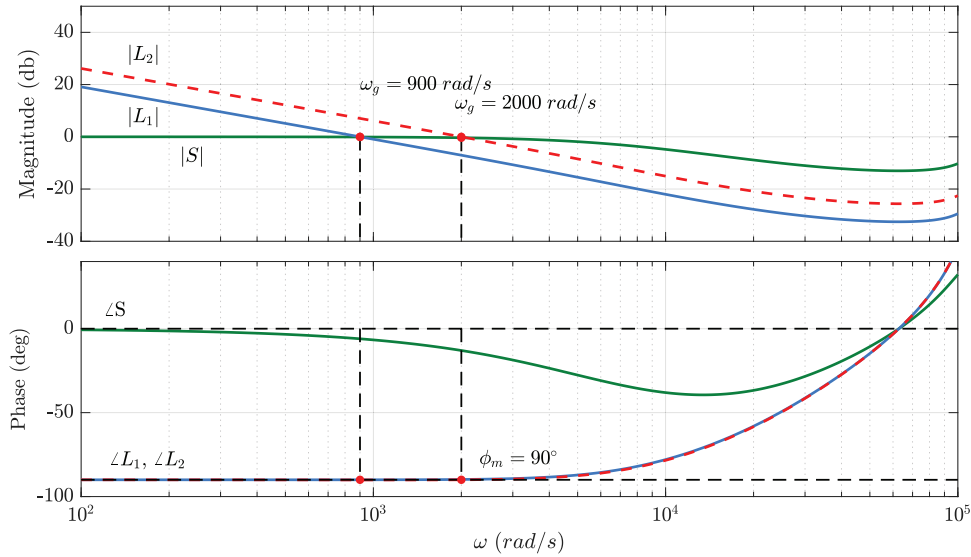
**FIGURE 18**    The Bode plots of the discrete-time system $S(\omega, T_s)$ and the loop gain frequency responses $L_1(\omega, T_s)$ and $L_2(\omega, T_s)$ under the design specifications $\phi_m = 90°$, $\omega_g = 900$ rad/s and $\omega_g = 2000$ rad/s.
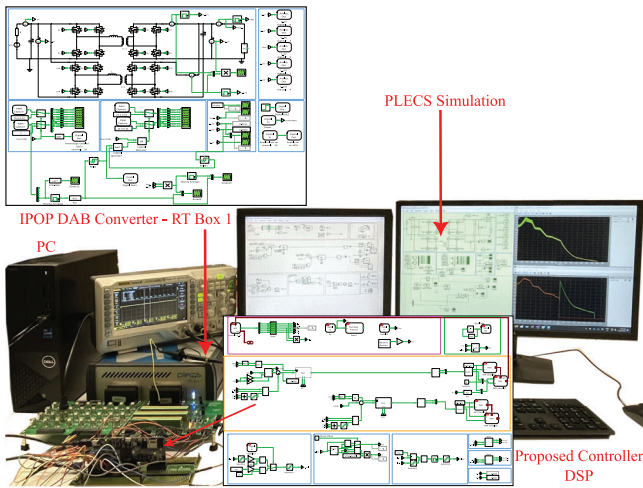


**FIGURE 19**    Real-time HIL experimental setup.

in the PLECS environment, taking into account a discretization step size of 5 $\mu$s for the converter and 50 $\mu$s for the controller. A power relay similar to the one discussed in Section 4.4 has been used.

## 5.1 | CC–CV charge mode control

Similar to what was done in the simulation results, the effectiveness of the proposed control has been verified under the same $I_{ref}$ step variation, i.e. from 120 to 150 A, meeting $\phi_m = 90°$, $\omega_g = 2000$ rad/s. The real-time HIL results in comparison with the offline classical procedure method are shown in Figure 20. The proposed control structure leads to a fast step response without overshoot, while the classical procedure

tracks the new reference value in more than 2 s, confirming the simulation results.

Similarly, the performance of the two-parallel PI method and the proposed method are evaluated through HIL tests. The PI parameters employed in the simulation were also utilized in the HIL tests for the two-parallel PI method. Figure 21 illustrates the HIL results for both the parallel PI control and the proposed control. Note that the undershoot of the output voltage and current at the switching instant with parallel PI have been doubled, while no perturbation has been obtained with the proposed control.

## 5.2 | Power charge mode control

The power profile of a Fiat 500e vehicle battery charging process (60 min) obtained from [42], has been used as the reference signal of IPOP converter in HIL tests. The given power profile, the output and inductor currents, and measured output power are shown in Figure 22. In particular, Figure 22(a) shows the output currents $i_{21}$ and $i_{22}$. The zoom in the top right corner shows the soft engagement of the second module at the beginning of the process. This is driven when the output power reaches 42.5 kW. It can be seen that this mode change is achieved without oscillations or overshoots. Then, during power-sharing mode, the output currents of the two modules are perfectly balanced. The module shedding is driven when the power is less than 40 kW and occurs after 30 min of charging. Also in this case the output current split into only a single module without oscillations or overshoots. Note that the inductor currents shown in Figure 22(b) are perfectly balanced during power-sharing mode and current overshoots are avoided during module shedding. The given power profile and the measured output power are shown in Figure 22(c). The proposed control
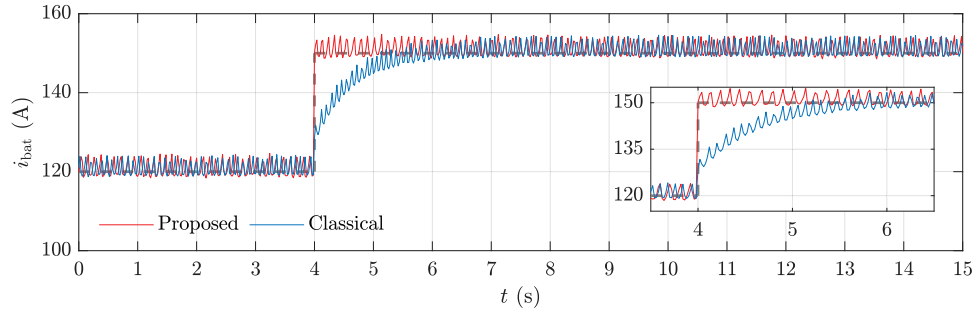
**FIGURE 20**  Battery current 120–150 A step variation under $\phi_m = 90°$, $\omega_g = 2000$ rad/s with the proposed method and under $\omega_n = 5$, $\zeta = 1$ with classical method.
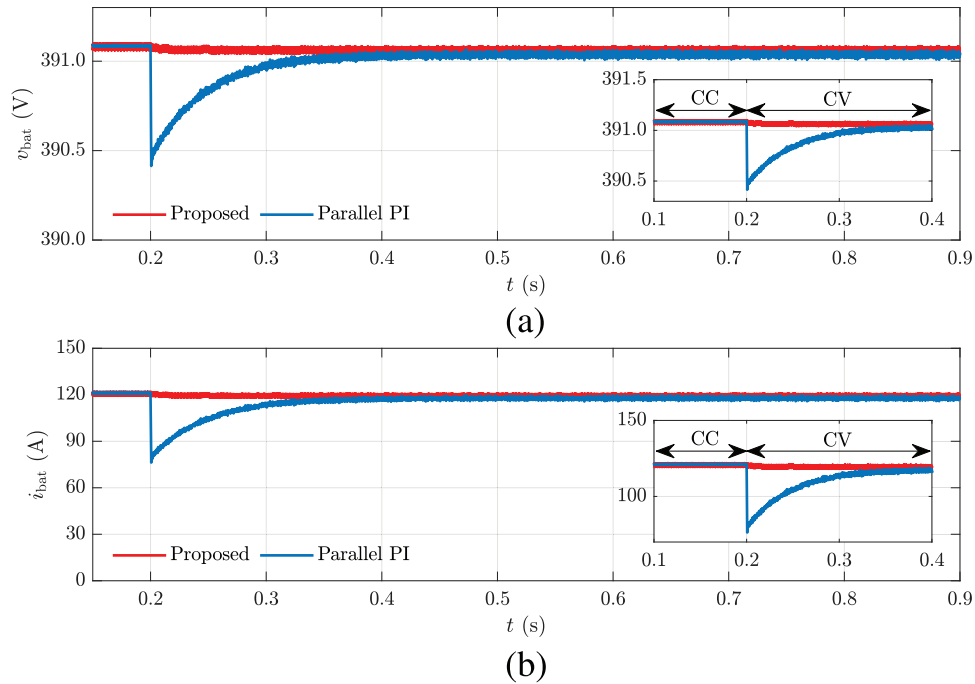


**FIGURE 21**  CC–CV mode switch: (a) battery output voltage; (b) current with the proposed method and with two parallel PI controllers.

perfectly tracks the given reference signal without perturbations during transient modes.

## 6 | CONCLUSION

This paper proposes a novel and unified battery charging control strategy in two-module and/or $N$-module IPOP DAB DC-DC converters for CC, CV, and power mode battery charging. The detailed mathematical derivation on achieving model-based autotuning PI parameters has been provided. The proposed simple closed-form formulae have the main advantage of being directly implemented by discrete microcontrollers as DSP without using offline trial and error procedures, and having the knowledge of the DAB model. Different test results have been shown by implementing the proposed controller and two-module IPOP DAB converter in PLECS simulation and

further verified through the real-time HIL procedure. The control system provides the expected good performance in the simulations, resulting in 4 and 1.8 ms settling time in long and small step variations. The same results are achieved even with considered large differences in battery parameters and DAB modules. The comparison with classical offline model-based pole placement methodology shows the advantages of using the proposed auto-tuning algorithm. The settling time of the classical pole placement method resulted in more than 1 s compared to the proposed method in the simulations whereas a precise settling time is observed during the HIL tests. Furthermore, the proposed controller proved its effectiveness in comparison with the parallel PI controller during the CC–CV switching instant. The presented soft module engagement, disengagement, and complete module shedding control are driven during an entire battery charging process without output current oscillation or overshoot in both simulation and HIL tests. These findings
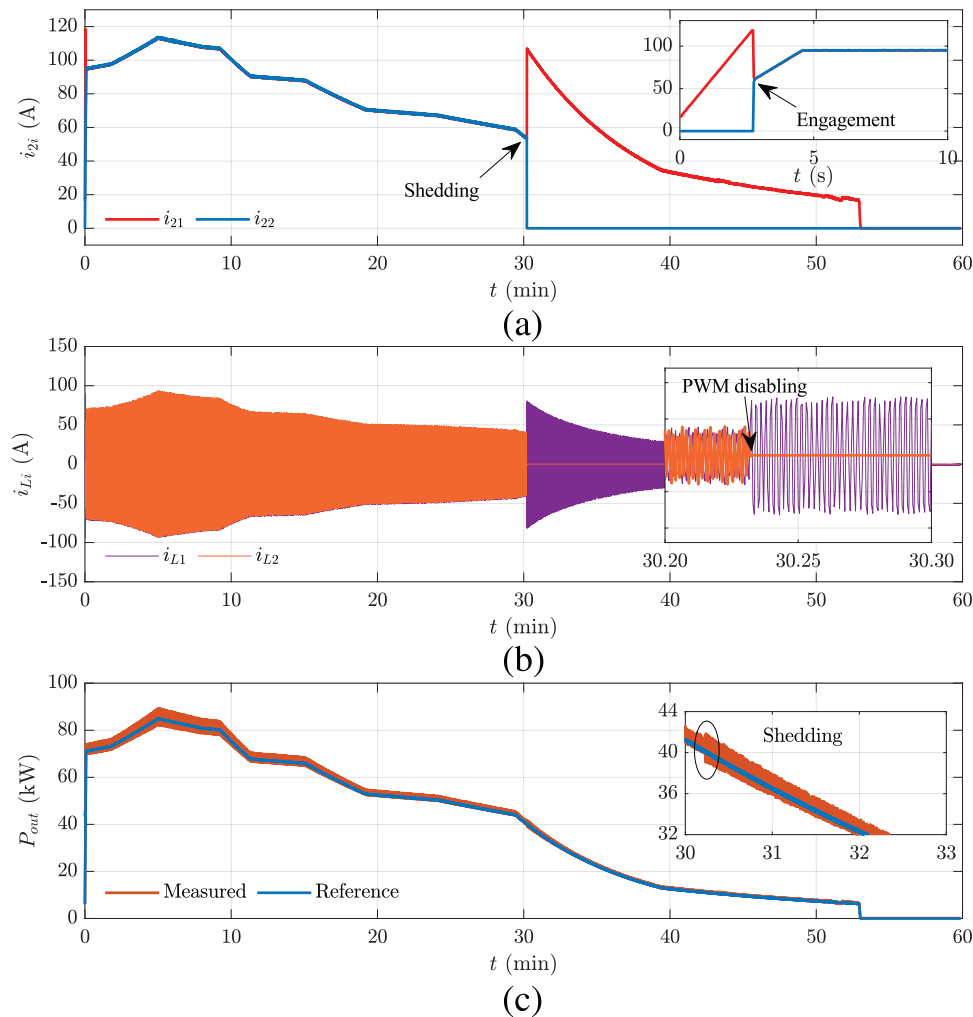
**FIGURE 22**   Real-time power profile of a Fiat 500e: (a) output currents; (b) inductor currents; (c) power.

highlight the pivotal role of the proposed control strategy in enhancing converter efficiency and advancing battery charging technologies in electric vehicles.

## AUTHOR CONTRIBUTIONS

**Stefania Cuoghi**: Conceptualization; formal analysis; investigation; writing—original draft; writing—review and editing. **Lohith Pittala**: Data curation; investigation; resources; software; validation; visualization; writing—original draft; writing—review and editing. **Riccardo Mandrioli**: Formal analysis; methodology; project administration; supervision; validation; writing—original draft; writing—review and editing. **Vincenzo Cirimele (GE)**: Project administration; resources; supervision; writing—original draft; writing—review and editing. **Mattia Ricco**: Funding acquisition; project administration; supervision; writing—original draft; writing—review and editing. **Gabriele Grandi**: Funding acquisition; project administration; supervision.

## CONFLICT OF INTEREST STATEMENT
The authors declare no conflicts of interest.

## DATA AVAILABILITY STATEMENT
Data sharing not applicable – no new data generated.

## ORCID
*Stefania Cuoghi* https://orcid.org/0000-0003-3415-0069
*Lohith Kumar Pittala* https://orcid.org/0000-0001-6563-9786
*Riccardo Mandrioli* https://orcid.org/0000-0003-3015-4150
*Vincenzo Cirimele* https://orcid.org/0000-0003-1999-0107
*Mattia Ricco* https://orcid.org/0000-0002-7482-1173
*Gabriele Grandi* https://orcid.org/0000-0002-4565-1064

# REFERENCES

1. Brenna, M., Foiadelli, F., Leone, C., Longo, M.: Electric vehicles charging technology review and optimal size estimation. J. Electr. Eng. Technol. 15, 2539–2552 (2020)

2. Acharige, S.S.G., Haque, M.E., Arif, M.T., Hosseinzadeh, N., Hasan, K.N., Oo, A.M.T.: Review of electric vehicle charging technologies, standards, architectures, and converter configurations. IEEE Access 11, 41 218–41 255 (2023)

3. Li, L., Xu, G., Sha, D., Liu, Y., Sun, Y., Su, M.: Review of dual-active-bridge converters with topological modifications. IEEE Trans. Power Electron. 38(7), 9046–9076 (2023)

4. Habib, S., Khan, M.M., Abbas, F., Ali, A., Faiz, M.T., Ehsan, F., Tang, H.: Contemporary trends in power electronics converters for charging solutions of electric vehicles. CSEE J. Power Energy Syst. 6(4), 911–929 (2020)

5. Rolak, M., Sobol, C., Malinowski, M., Stynski, S.: Efficiency optimization of two dual active bridge converters operating in parallel. IEEE Trans. Power Electron. 35(6), 6523–6532 (2020)

6. Sun, K., Su, M., Xu, G., Chen, X., Xiong, W.: Modulated coupled inductor based IPOP-DAB converter with optimized modulation trajectory considering the phase-shift angle between sub-modules for SST applications. IEEE J. Emerg. Sel. Top. Power Electron. 11(6), 6112–6123 (2023)

7. Alharbi, M.A., Alcaide, A.M., Dahidah, M., P., M.-R., Ethni, S., Pickert, V., Leon, J.I.: Rotating phase shedding for interleaved DC-DC converter-based EVs fast DC chargers. IEEE Trans. Power Electron. 38(2), 1901–1909 (2023)

8. Peyghami, S., Wang, Z., Blaabjerg, F.: A guideline for reliability prediction in power electronic converters. IEEE Trans. Power Electron. 35(10), 10 958–10 968 (2020)

9. Panov, Y., Jovanovic, M.: Stability and dynamic performance of current-sharing control for paralleled voltage regulator modules. IEEE Trans. Power Electron. 17(2), 172–179 (2002)

10. Li, D., Man Ho, C.N.: A delay-tolerable master-slave current-sharing control scheme for parallel-operated interfacing inverters with low-bandwidth communication. IEEE Trans. Ind. Appl. 56(2), 1575–1586 (2020)

11. Kim, J.-W., Choi, H.-S., Cho, B.H.: A novel droop method for converter parallel operation. IEEE Trans. Power Electron. 17(1), 25–32 (2002)

12. Hou, N., Li, Y.W.: Overview and comparison of modulation and control strategies for a nonresonant single-phase dual-active-bridge DC-DC converter. IEEE Trans. Power Electron. 35(3), 3148–3172 (2020)

13. Pan, X., Yang, F., Li, L., Zhang, R., Wang, C.: An improved modulation scheme of active commutated current-fed bidirectional DC/DC converter. IEEE J. Emerg. Sel. Top. Power Electron. 9(2), 1375–1388 (2021)

14. Zhao, B., Song, Q., Liu, W., Sun, W.: Current-stress-optimized switching strategy of isolated bidirectional DC-DC converter with dual-phase-shift control. IEEE Trans. Ind. Electron. 60(10), 4458–4467 (2013)

15. Chen, X., Xu, G., Han, H., Liu, D., Sun, Y., Su, M.: Light-load efficiency enhancement of high-frequency dual-active-bridge converter under SPS control. IEEE Trans. Ind. Electron. 68(12), 12 941–12 946 (2021)

16. Chaurasiya, S., Singh, B.: A load adaptive hybrid DPS control for dab to secure minimum current stress and full ZVS operation over wide load and voltage conversion ratio. IEEE Trans. Ind. Appl. 59(2), 1901–1911 (2023)

17. Veeramraju, K.J.P., Kimball, J.W.: Dynamic model of AC-AC dual active bridge converter using the extended generalized average modeling framework. IEEE Trans. Power Electron. 39(3), 3558–3567 (2024)

18. Iqbal, M.T., Maswood, A.I.: An explicit discrete-time large- and small-signal modeling of the dual active bridge DC-DC converter based on the time scale methodology. IEEE J. Emerg. Sel. Top. Ind. Electron. 2(4), 545–555 (2021)

19. Shao, S., Chen, L., Shan, Z., Gao, F., Chen, H., Sha, D., Dragicević, T.: Modeling and advanced control of dual-active-bridge DC-DC converters: a review. IEEE Trans. Power Electron. 37(2), 1524–1547 (2022)

20. Iqbal, M.T., Maswood, A.I., Tafti, H.D., Tariq, M., Bingchen, Z.: Explicit discrete modelling of bidirectional dual active bridge DC-DC converter using multi-time scale mixed system model. IET Power Electron. 13(18), 4252–4260 (2020)

21. Zhao, W., Zhang, X., Gao, S., Ma, M.: Improved model-based phase-shift control for fast dynamic response of dual-active-bridge DC/DC converters. IEEE J. Emerg. Sel. Top. Power Electron. 9(1), 223–231 (2021)

22. Farooq, Z., Zaman, T., Khan, M.A., Nasimullah, Muyeen, S.M., Ibeas, A.: Artificial neural network based adaptive control of single phase dual active bridge with finite time disturbance compensation. IEEE Access 7, 112 229–112 239 (2019)

23. Fu, Y., Jing, Z., Ren, H.-P.: Model predictive control for DAB under extended-phase-shift considering components uncertainty. IET Power Electron. 16(12), 1984–1995 (2023)

24. Li, X., Dong, Z., Cao, Y., Qin, J., Zhang, Z., Tse, C.K., Wang, R.: Model-predictive control with parameter identification for multi-dual-active-bridge converters achieving accurate power balancing. IEEE Trans. Power Electron. 38(9), 10 880–10 894 (2023)

25. An, F., Song, W., Yu, B., Yang, K.: Model predictive control with power self-balancing of the output parallel DAB DC-DC converters in power electronic traction transformer. IEEE J. Emerg. Sel. Top. Power Electron. 6(4), 1806–1818 (2018)

26. Ji, L., Zhang, M., Qian, B., Sun, H.: A series of hybrid WPT systems with automatic switching between constant-current and constant-voltage modes on the secondary side. IEEE J. Emerg. Sel. Top. Power Electron. 11(1), 361–371 (2023)

27. Cuoghi, S., Mandrioli, R., Pittala, L.K., Cirimele, V., Ricco, M.: Dual-active-bridge model and control for supporting fast synthetic inertial action. Energies 15(6), 2295 (2022)

28. Cuoghi, S., Mandrioli, R., Ntogramatzidis, L., Gabriele, G.: Multileg interleaved buck converter for EV charging: discrete-time model and direct control design. Energies 13(2), 466 (2020)

29. Liu, X., Zhu, Z.Q., Stone, D.A., Foster, M.P., Chu, W.Q., Urquhart, I., Greenough, J.: Novel dual-phase-shift control with bidirectional inner phase shifts for a dual-active-bridge converter having low surge current and stable power control. IEEE Trans. Power Electron. 32(5), 4095–4106 (2017)

30. Bai, H., Mi, C.: Eliminate reactive power and increase system efficiency of isolated bidirectional dual-active-bridge DC-DC converters using novel dual-phase-shift control. IEEE Trans. Power Electron. 23(6), 2905–2914 (2008)

31. Mandrioli, R., Ricco, M., Grandi, G., Pereira, T.A., Liserre, M.: Dab-based common-mode injection in three-phase four-wire inverters. In: Proceedings of IEEE International Conference Compatibility, Power Electronics, and Power Engineering (CPE-POWERENG), pp. 1–6. IEEE, Piscataway, NJ (2022)

32. Fan, S., Li, Y., Yuan, Y., Hu, X., Dai, W.: Comparative analysis of isolated bidirectional dual-active-bridge DC-DC converter based on EPS and DPS. In: 2019 22nd International Conference on Electrical Machines and Systems (ICEMS), pp. 1–6. IEEE, Piscataway, NJ (2019)

33. Hou, N., Li, Y.: The comprehensive circuit-parameter estimating strategies for output-parallel dual-active-bridge DC-DC converters with tunable power sharing control. IEEE Trans. Ind. Electron. 67(9), 7583–7594 (2020)

34. Cuoghi, S., Ntogramatzidis, L.: Direct and exact methods for the synthesis of discrete-time proportional-integral-derivative controllers. IET Control. Theory Appl. 7(18), 2164–2171 (2013)

35. Arora, S., Singh, M.: Reduction of switching transients in CC/CV mode of electric vehicles battery charging. In: 5th IET International Conference on Clean Energy and Technology (CEAT2018), pp. 1–6. IEEE, Piscataway, NJ (2018)

36. Meng, J., Ricco, M., Luo, G., Swierczynski, M., Stroe, D.-I., Stroe, A.-I., Teodorescu, R.: An overview and comparison of online implementable SOC estimation methods for lithium-ion battery. IEEE Trans. Ind. Appl. 54(2), 1583–1591 (2018)

37. Ogata, K.: Modern Control Engineering, 4th Edition. Prentice Hall, Hoboken, NJ (2001)

38. Fang, Z., Yue, H., Wei, Z., Zhang, Z., Huang, Z.: A control-free series resonant converter for battery charging with automatic CC-to-CV profile and whole-process high efficiency. IEEE Trans. Power Electron. 38(7), 8666–8675 (2023)

39. Park, K.-H., Choi, Y.-J., Choi, S.-Y., Kim, R.-Y.: Design consideration of CC-CV controller of LLC resonant converter for Li-ion battery charger. In: IEEE 2nd International Future Energy Electronics Conference (IFEEC), pp. 1–6. IEEE, Piscataway, NJ (2015)

40. Hoque, M.M., Hannan, M.A., Mohamed, A.: Optimal CC-CV charging of lithium-ion battery for charge equalization controller. In: International Conference on Advances in Electrical, Electronic and Systems Engineering (ICAEES), pp. 610–615. IEEE, Piscataway, NJ (2016)

41. Rolak, M.: Avoiding currents overshoot in ipop dab system. In: Proceedings of IEEE International Conference on Industrial Technology (ICIT), pp. 1737–1742. IEEE, Piscataway, NJ (2019)

42. Franco, F.L., Ricco, M., Cirimele, V., Apicella, V., Carambia, B., Grandi, G.: Electric vehicle charging hub power forecasting: a statistical and machine learning based approach. Energies 16(4), 2076 (2023)